# Supporting Information

## Simulation and Fabrication of Nanoscale Spirals Based on Dual-Scale Self-Assemblies

Gun Ho Lee,[†] Shinho Kim,[‡] YongJoo Kim,*[,§] Min Seok Jang,*[,‡] Yeon Sik Jung*[,†]

[†] Department of Materials Science and Engineering, Korea Advanced Institute of Science and Technology (KAIST), 291 Daehak-ro, Yuseong-gu, Daejeon 34141, Republic of Korea

[‡] School of Electrical Engineering, Korea Advanced Institute of Science and Technology (KAIST), 291 Daehak-ro, Yuseong-gu, Daejeon 34141, Republic of Korea

[§] School of Materials Science and Engineering, Kookmin University, 77 Jeongneung-ro, Seongbuk-gu, Seoul 02707, Republic of Korea

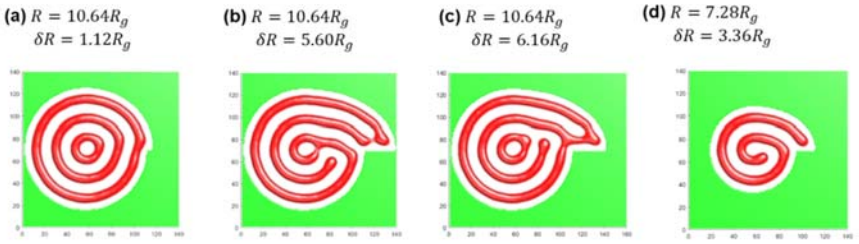


**Figure S1.** SCFT simulation results for self-assembly of cylinder-forming BCPs in asymmetric circular trench structures with defect. The circular trenches have geometries of (a) $R = 10.64R_{\mathrm{g}}$ and $\delta R = 1.12R_{\mathrm{g}}$, (b) $R = 10.64R_{\mathrm{g}}$ and $\delta R = 5.60R_{\mathrm{g}}$, (c) $R = 10.64R_{\mathrm{g}}$ and $\delta R = 6.16R_{\mathrm{g}}$, and (d) $R = 7.28R_{\mathrm{g}}$ and $\delta R = 3.36R_{\mathrm{g}}$

Figure S1 shows SCFT simulation results for BCP behavior in a number of templates omitted in Figure 1. In templates with small $\delta R$, BCP overcomes the free energy barrier from lattice mismatch with small distortions in the outermost ring but maintains the concentric ring structure, as shown in Figure S1a. This morphology is seen in templates with defect size up to $\delta R = 2.24R_{\mathrm{g}}$(Figure 1e), but a disconnecting defect is produced to form spiral morphology when the defect is further stretched to $\delta R = 2.80R_g$ (Figure 1f). Figure S1b,c show that further increases in $\delta R$ result in significant distortions in the spiral morphology, such as formation of two spirals ends at the defect (Figure S1b) or an island in the central region (Figure S1c). These results show that the defect size has a significant influence on the formation of spirals in these templates and that stable formations of spirals occur in templates with defect size between $2.80R_{\mathrm{g}}$ and $4.48R_{\mathrm{g}}$, a range in which a single cylinder would form within the defect. Figure S1d, on the other hand, exhibits formation of a $4\pi$ spiral produced by decreasing the radius to $R = 7.28R_{\mathrm{g}}$ while maintaining the defect size at $\delta R = 3.36R_{\mathrm{g}}$. This shows that self-assemblies into spirals of various winding numbers are stable in trenches of corresponding R when the defect size $\delta R$ is approximately $\mathrm{L}_0$.

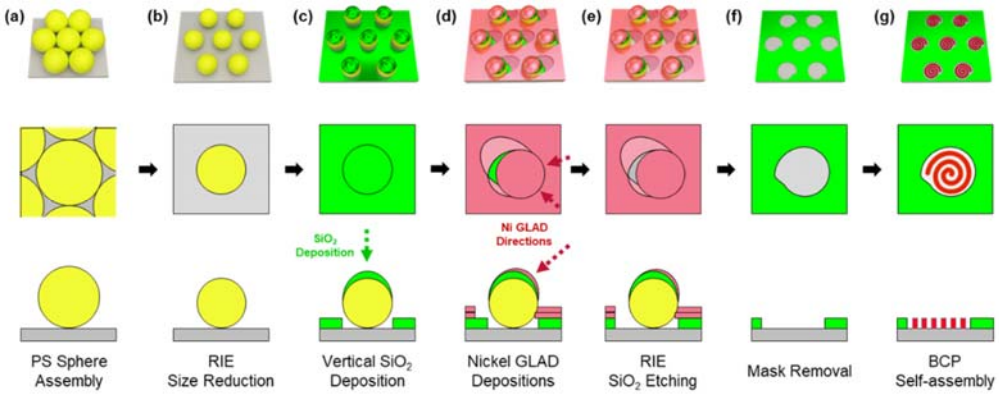


**Figure S2.** Overview of template fabrication process. Each row illustrates three-dimensional illustration, bird's eye view, and cross-sectional view of samples in each step, respectively from the top. Schematics for (a) polystyrene nanosphere monolayer self-assembly, (b) size reduction using ICP-RIE, (c) vertical deposition of $SiO_2$, (d) two-step GLAD of nickel etch masks, (e) anisotropic dry etching of $SiO_2$ using ICP-RIE, (f) nickel and PS sphere removal, and (g) block copolymer self-assembly within the trenches.

Figure S2 illustrates schematics for the fabrication process from different perspectives for more detailed descriptions of the process. Figure S2a,b respectively show capillary-force-induced self-assembly of PS nanospheres into a hexagonally close-packed monolayer and their size reduction using ICP-RIE. As mentioned in Results and Discussion, the dry etching process allows precise size reduction of the PS nanospheres, which determines the radius $R$ of the template. In Figure S2c-e, an electron beam evaporator is used to vertically deposit a $SiO_2$ layer, followed by two-step consecutive glancing angle deposition (GLAD) of nickel etch mask layers. The GLAD directions are portrayed in the schematic. The GLAD technique produces crescent-shaped shadows, and the bird's eye view schematic in Figure S2d shows how two dissimilarly shaped shadows in different directions form an overlapping region that functions as an asymmetric nanohole. Subsequently, an anisotropic dry etching process, using ICP-RIE with high bias power, is used to selectively etch the $SiO_2$ layer exposed by the nanohole. The PS nanospheres and nickel layers function as etch masks in this process, allowing an asymmetric defect to be formed adjacent to the circular template. Nanospheres and nickel layers are then removed with ultra-sonication and wet etching treatments, respectively, completing the template fabrication process. BCP self-assembly is induced within the fabricated asymmetric templates, forming spiral nanostructures, as shown in Results and Discussion.

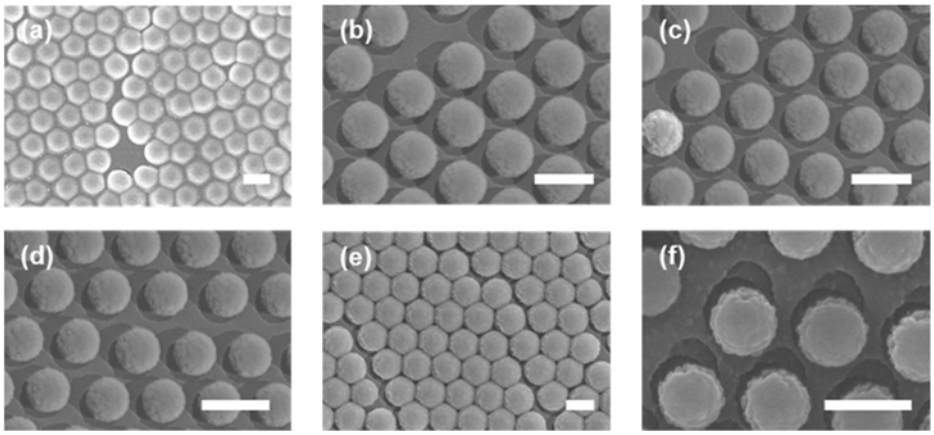


**Figure S3.** Size and pattern period control of the templates. SEM images of hexagonally close-packed PS microspheres with inductively coupled plasma reactive-ion etching (ICP-RIE) process and deposition: radius of (a) 250 nm as spun, (b) 250 nm etched to 200 nm, (c) 250 nm etched to 180 nm, (d) 250 nm etched to 160 nm, (e) 100 nm as spun, and (f) 100 nm etched to 80 nm. The scale bars in (a)-(d) and (e)-(f) represent 500 and 200 nm, respectively.

Figure S3 shows images of the size and pattern period modification of the templates using polystyrene (PS) microspheres. As the initial step of the fabrication process, a hexagonally close-packed monolayer of PS microspheres is formed on a silicon substrate using capillary force assembly and etched with ICP-RIE process with $O_2$ plasma (15 mTorr, 100/5 W) to reduce their size. As can be seen in the SEM images above, the radius of the etched microspheres determines the radius of the circular parts of the trenches, $R$. Meanwhile, the initial radius of the microspheres determines the pattern period, or the center-to-center distances between neighboring trenches. For example, microspheres used in Figure S3a-d have an initial radius of 250 nm prior to the ICP-RIE procedure, and arrays fabricated using these microspheres have pattern periods of 500 nm. Microspheres used in Figure S3e and S3f, on the other hand, have initial radius of 100 nm, resulting in a pattern periods of 200 nm.

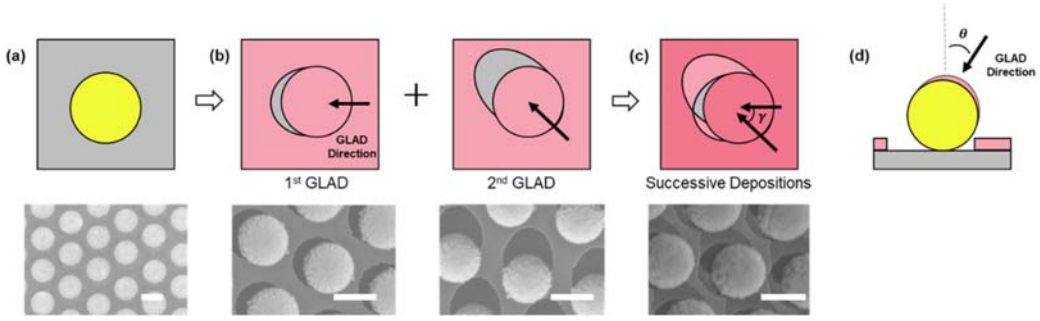


**Figure S4.** Two-step angled deposition technique for asymmetric nanohole fabrication. Schematics and SEM images for (a) polystyrene nanospheres after size reduction. (b) Two-step GLAD process. (c) Resultant deposition layers. (d) Cross-sectional view of GLAD. Scale bars represent 300 nm.

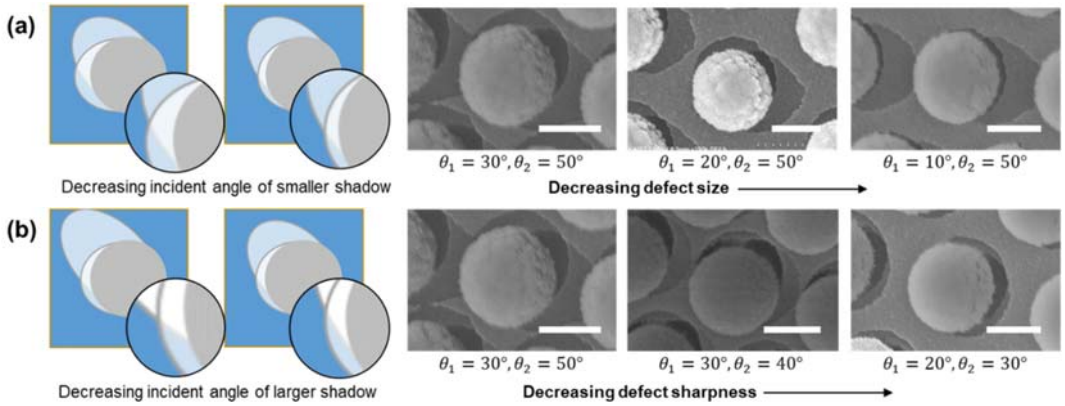


**Figure S5.** Effect of glancing angles of deposition on size and shape of the defect. Schematics and SEM images of (a) effect of glancing angle $\theta_1$ for the smaller shadow and (b) effect of glancing angle $\theta_2$ for the larger shadow. Scale bars represent 200 nm.

Glancing angle deposition (GLAD) on a spherical structure produces a crescent-shaped shadow. We discovered that when two deposition shadows with dissimilar shapes are formed with consecutive GLADs in different angles and directions, the overlapped portion, where deposition has not occurred both times, has an asymmetric silhouette and forms a nanohole in the nickel layer. The glancing angle, termed $\theta$ and depicted in the cross-sectional schematic in Figure S4d, describes the deposition angle from the surface normal and determines the size and shape of the shadow, as shown in Figure S4b. Meanwhile, the azimuthal angle between the 1st and 2nd GLAD directions, termed $\gamma$ and depicted in Figure S4c, determines the nanohole shape. This nanohole is used as the etch mask to selectively etch the underlying $SiO_2$ to fabricate the asymmetric defect.

Figure S5 shows how the glancing angles affect the size and shape of the defect. As mentioned above, the glancing angle $\theta$ of incident deposition flux affects the size of the shadow. In making the asymmetric nanohole, glancing angles of the smaller and larger shadows affect the nanohole shape in

different manners. As can be seen in Figure S5a, the glancing angle for the smaller shadow, termed $\theta_1$, determines the size of the overlapping portion, which consequently affects $\delta R$. A smaller $\theta_1$ leads to a smaller $\delta R$. Figure S5b, on the other hand, shows how the glancing angle for the larger shadow, termed $\theta_2$, determines the shape of the overlapped portion. A larger $\theta_2$ leads to a more asymmetric defect with a sharper edge. However, $\theta_2$ should not be too large as it may affect neighboring templates when the shadow is too large. Furthermore, experimental evaluations show that the difference between $\theta_1$ and $\theta_2$ should be maintained at $\theta_2 - \theta_1 \geq 20°$ in order to develop asymmetric defects.

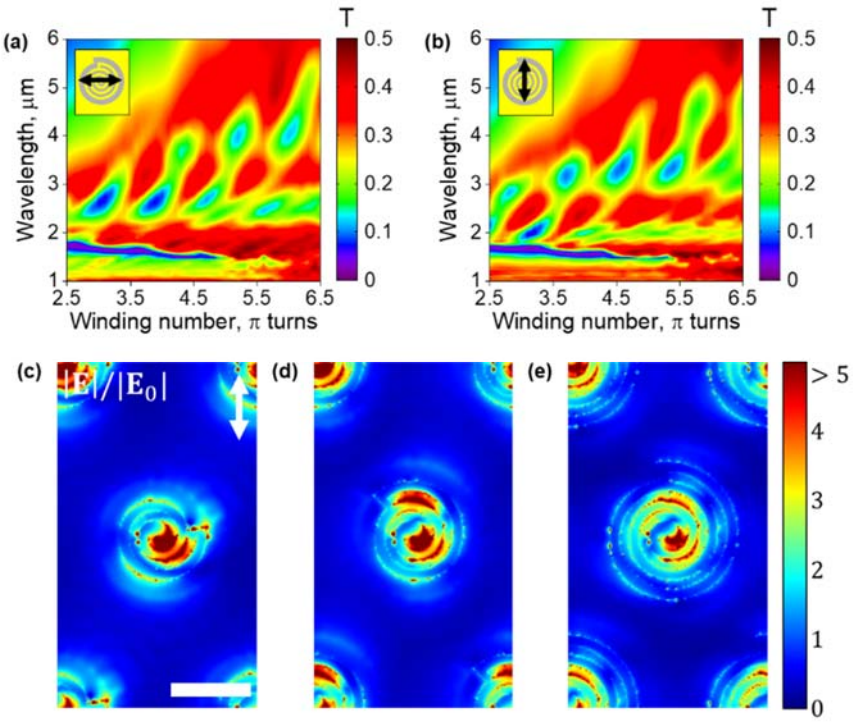


**Figure S6.** The calculated transmittance of $5.5\pi$ nanospiral array as a function of winding number and wavelength for (a) x-polarized and (b) y-polarized incident wave. The electric field distributions of nanospiral arrays with (c) $\Phi = 3.0\pi$, (d) $\Phi = 3.7\pi$, and (e) $\Phi = 5.5\pi$ at the maximum field enhancement wavelengths $\lambda = 1.95$ μm, 1.91 μm, and 1.92 μm, respectively. The scale bar represents 200 nm.

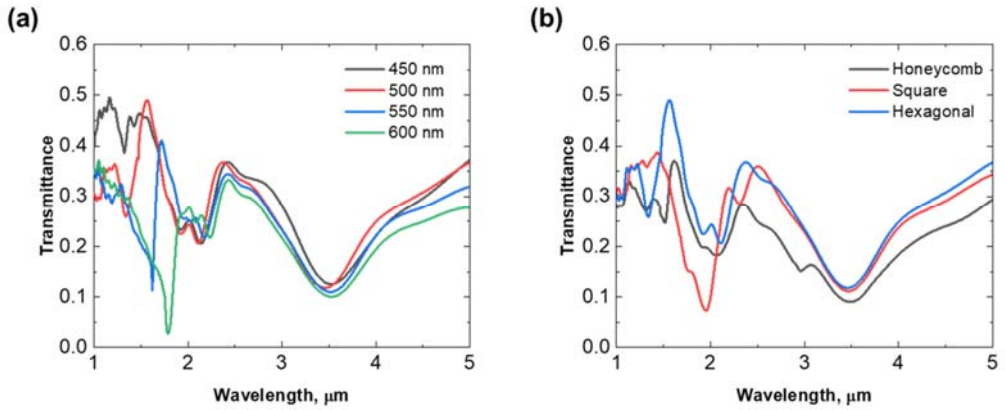


**Figure S7.** The calculated transmittance of 5.5π nanospiral arrays. (a) Comparison of hexagonally close-packed arrays with a range of lattice spacings and (b) comparison of close-packed arrays with lattice spacings of 500 nm in various packing geometries.